ELSEVIER

Contents lists available at ScienceDirect

## Journal of Solid State Chemistry

journal homepage: www.elsevier.com/locate/jssc





# Combustion synthesis of Eu<sub>2</sub>O<sub>3</sub> nanomaterials with tunable phase composition and morphology

Jordan M. Roach <sup>a</sup>, Khachatur V. Manukyan <sup>b,\*</sup>, Stefania Dede <sup>b,c</sup>, Peter C. Burns <sup>a,d</sup>, Ani Aprahamian <sup>a,b,e</sup>

- <sup>a</sup> Department of Chemistry and Biochemistry, University of Notre Dame, Notre Dame, IN, 46556, United States
- b Nuclear Science Laboratory, Department of Physics & Astronomy, University of Notre Dame, Notre Dame, IN, 46556, United States
- Cyclotron Institute, Texas A&M University, College Station, TX, 77843, United States
- d Department of Civil & Environmental Engineering & Earth Sciences, University of Notre Dame, Notre, Dame, IN, 46556, United States
- <sup>e</sup> A. Alikhanyan National Science Laboratory of Armenia, 2 Alikhanyan Brothers, 0036, Yerevan, Armenia

#### ARTICLE INFO

### Keywords: Europium (III) oxide Solution combustion synthesis Nanoparticles Thin films phase changes

#### ABSTRACT

Combustion reactions in europium nitrate – acetylacetone – 2-methoxyethanol solutions and gels were investigated to produce europium (III) oxide ( $Eu_2O_3$ ) nanocrystalline materials and thin films. Thermal analyses of solutions indicated that the 2-methoxyethanol solvent also acts as a fuel in the absence of acetylacetone. Adding acetylacetone increases the overall heat of the reaction. Thermal analysis results revealed that the slow oxidation of unburned hydrocarbon residues follows the primary combustion reaction. Time-temperature profile measurements of the bulk combustion synthesis process in air and nitrogen atmospheres enabled the extraction of the maximum reaction temperature and the heating and cooling rates in the combustion zone. Several direct correlations exist between measured combustion parameters and the phase composition of the products. Combustion in air results in mixed-phase cubic and monoclinic nanocrystalline  $Eu_2O_3$ . Increasing the acetylacetone concentration in solutions increases the synthesis temperature and decreases the quantity of cubic  $Eu_2O_3$ . The reaction of solutions in a nitrogen atmosphere or diluted with  $Eu_2O_3$  provides control of the product phase composition and reduces the quantity of the monoclinic phase. Transmission electron microscopy imaging shows that the  $Eu_2O_3$  end products are highly porous aggregates of nanocrystalline particles. Electrospraying of reactive solutions onto different substrates followed by short annealing makes the preparation of  $Eu_2O_3$  materials with diverse morphologies possible.

### 1. Introduction

Rare earth elements (REEs), including lanthanides, yttrium, and scandium, are essential for the production of electronics [1,2], catalysts [3], medicine [4], and magnetic materials [5,6], among others. These elements have similar chemical properties and occur in small quantities within the same ores and spent nuclear fuel [7-13]. Cation exchange and organic complexation are the primary methods of separating REEs from actinides [14]. After such separation steps, the resulting solutions contain mixtures of REEs. The chemical separation of individual REEs takes numerous repetitive stages using solvents to achieve adequate purity [15-17]. Chemically separated REE solutions are converted to mainly trivalent sesquioxides by furnace annealing at temperatures above 1200 K [18-21].

REE sesquioxides offer unique physical and chemical properties [22–26]. These oxides commonly exhibit hexagonal (A type), monoclinic (B), and cubic (C) polymorphs [24,27–32].  $\rm Eu_2O_3$  is particularly interesting owing to its electronic properties that occur in only the B- or C- polymorphs at ambient pressure [21,33–36]. The different phases of  $\rm Eu_2O_3$  can be utilized in various applications for optics and electronics, including optical waveguides, filters, and capacitors. However, the impact of polymorphic structure on the physical characteristics of  $\rm Eu_2O_3$  remains unknown. In addition, creating  $\rm Eu_2O_3$  films with controlled phase composition on different substrates is highly beneficial for producing thin film target materials for nuclear science measurements, catalysis, and electronics research purposes. Pure phase C- and B–Eu<sub>2</sub>O<sub>3</sub> are predominantly produced by time- and energy-intensive furnace annealing [18–21]. The B–Eu<sub>2</sub>O<sub>3</sub> polymorph exclusively forms upon

E-mail address: kmanukya@nd.edu (K.V. Manukyan).

<sup>\*</sup> Corresponding author.

annealing C-Eu<sub>2</sub>O<sub>3</sub> at temperatures ranging from 1323 to 1623 K [30].

Solution combustion synthesis (SCS) is a rapid and energy-efficient method to produce nanoscale oxides [37–42]. These self-sustaining, exothermic reactions use organic compounds (fuel) to convert metal nitrates (oxidizers) to their corresponding oxides. The most frequently used fuels are water-soluble organic compounds, such as glycine [43], urea [44], glucose [45], and hexamethylenetetramine [46]. Modification of the fuel-to-oxidizer ratio ( $\varphi$ ) provides control over product phase composition. SCS is broadly used with spin coating and spraying methods to prepare thin films [47–50]. Unlike traditional fuel and solvents used in bulk SCS, acetylacetone and 2-methoxyethanol are used as fuel and solvents in thin film preparation [52,53]. These compounds have similar boiling temperatures, and 2-methoxyethanol can serve as both fuel and solvent. However, the role of these compounds and their specific functions in the combustion synthesis mechanism is unknown.

This work reports a simple and rapid combustion synthesis of  $\rm Eu_2O_3$  nanoscale materials and thin films using  $\it europium$   $\it nitrate + acetylacetone + 2-methoxyethanol$  solutions. Thermal analysis and temperature-profile measurements of bulk combustion precursor solutions enabled probing the combustion reaction mechanism with and without acetylacetone fuel. Combustion of bulk solutions without acetylacetone produces mixed-phase C- and B–Eu $_2O_3$  nanomaterials. Incorporating acetylacetone with varying ratios results in an overall increase in B–Eu $_2O_3$  concentration. The synthesis process performed under a nitrogen atmosphere and/or diluting the solutions with Eu $_2O_3$  product, shows a decrease in the overall content of the B-phase. Depositing reactive solutions on different substrates, followed by an annealing step, facilitates the preparation of pure C–Eu $_2O_3$  with unique morphologies and thin films.

## 2. Experimental

## 2.1. Materials synthesis and processing

## 2.1.1. Bulk combustion synthesis

A schematic representation of combustion methods used and major experimental steps are summarized in the Supplemental Information (Fig. S1). Acetylacetone (C<sub>5</sub>H<sub>8</sub>O<sub>2</sub>, TCI, >99.0%), 2-methoxyethanol (Alfa Aesar, 99%), and europium nitrate hexahydrate (Eu  $(NO_3)_3 \cdot 6H_2O$ , Alfa Aesar, 99.9%) were used as reactants. Eu (NO<sub>3</sub>)<sub>3</sub>·6H<sub>2</sub>O was dissolved in 2-methoxyethanol to prepare a 0.5 M reactive stock solution. 2.0 mL aliquots of stock solution were transferred to 4 mL glass vials. Desired amounts of C5H8O2 were added, and the solutions were mixed. The molar ratio (φ) of C<sub>5</sub>H<sub>8</sub>O<sub>2</sub> to Eu (NO<sub>3</sub>)<sub>3</sub>·6H<sub>2</sub>O was varied from 0.0 to 0.7. The solutions were heated to 400 K to form gels with a total volume of  $\sim$ 0.5 mL (8–10 h). Reactions were initiated using a hotplate, with precursor gels placed on a glass petri dish for open-air combustion or into a quartz reaction vessel purged with nitrogen for inert atmosphere combustion. Experiments with serial dilutions were performed via mixing (10% w/w) of the combustion product (Eu<sub>2</sub>O<sub>3</sub>) with a  $\varphi = 0.0$  precursor gel, i.e., Eu(NO<sub>3</sub>)<sub>3</sub>·6H<sub>2</sub>O solutions in 2-methoxyethanol. Time-temperature profiles of the process were measured using K-type thermocouples (100 µm diameter) and a DT9828 data acquisition system at a frequency of 100 Hz.

## 2.1.2. Spraying-assisted combustion synthesis

 $Eu_2O_3$  nanomaterials were also prepared by electrospraying  $Eu~(NO_3)_3+\phi C_5H_8O_2+2$ -methoxyethanol solutions  $(\phi=0.5~{\rm or}~0.6~{\rm ratios})$  using a previously described method [47,51]. Briefly, a mirror-finished aluminum alloy (6061, with impurities: Cr 0.04–0.35%, Cu 0.15–0.4%, Fe < 0.7%, Mn < 0.15%, Si 0.4–0.8%, Ti < 0.15%, Zn < 0.25%, and Mg 0.8–1.2 wt%) or boron-doped polished silicon wafers were used as substrates. Substrate wettability was modified using oxygen plasma, ozone pretreatment, or hexamethyldisilazane deposition. The solutions were sprayed with a 20  $\mu L/h$  flow rate for 20–90 min. 15 kV high voltage was applied between the stainless-steel nozzle (0.25 mm inner diameter)

and substrate, positioned  $\sim$ 7.5 cm apart. During deposition, the substrates were kept at 320 K. After spraying, samples were annealed at 623–873 K for 30 min to initiate the combustion reaction on thin layers of deposited solutions.

#### 2.1.3. Characterization methods

Thermal analysis of reactive solutions was conducted using thermogravimetric analysis-differential scanning calorimetry (TGA-DSC, Mettler-Toledo). 10  $\mu L$  aliquots of solutions were placed in 100  $\mu L$  aluminum crucibles and heated to 673 K at a rate of 25 K min $^{-1}$  with an airflow of 20 mL min $^{-1}$ . Powder X-ray diffraction (PXRD) patterns were measured for products using a Bruker D8 Discover diffractometer equipped with a Cu-K $\alpha$  radiation source and a LynxEye solid-state pixel detector. Patterns were collected over a 20 range of 15–80°, using a step size of 0.02°, and a scan rate of 5 s per step. The phase composition of powdered nanoscale products was quantified using Rietveld refinement of the PXRD patterns [54].

Scanning electron microscopy (SEM) was used to image the surface morphology of nanomaterials deposited on Si or Al substrates. A Helios Nanolab 600 (Thermo Fisher Scientific) with a dual electron/ion beam system was used for secondary-electron imaging. Purity of materials was examined using energy dispersive X-ray spectroscopy (EDS) using a JEOL JCM-6000 Plus Neoscope Benchtop SEM. The morphology and structure of the nanoscale materials were also investigated using a Spectra 300-300 (Thermo Scientific) transmission electron microscope (TEM) with a 30–50 p.m. resolution at 300 kV.

Surface area measurements and average pore sizes were obtained using an ASAP 2020 (Micrometrics) instrument, using Brunauer-Emmett-Teller (BET) and Barrett-Joyner-Halenda (BJH) analyses, respectively. Samples were degassed at 473 K for 200 min while under ultrahigh vacuum, followed by  $N_2$  isotherm data collection at 77 K.

## 3. Results and discussion

## 3.1. Thermal analysis

Thermal analysis of the stock solution of Eu(NO<sub>3</sub>)<sub>3</sub>·6H<sub>2</sub>O in 2-methoxyethanol before adding fuel ( $\phi=0$ ) revealed three distinct thermal events (Fig. 1A). An initial endothermic step associated with solvent evaporation was observed at 391 K ( $-270~J~g^{-1}$ ), followed by two exothermic peaks centered at 427 K ( $\alpha$ , 121 J g<sup>-1</sup>) and 548 K ( $\beta$ , 47 J g<sup>-1</sup>). Solvent evaporation accounts for a 71.7% mass loss, while the  $\alpha$  and  $\beta$  exotherm peaks correspond to 7.5% and 1.7% mass loss, respectively. The  $\alpha$  peak is assigned to the combustion of Eu(NO<sub>3</sub>)<sub>3</sub> with the solvent acting as a reducing fuel source. This broad peak has a shoulder on its left, indicating a multistep combustion process. The  $\beta$  peak appears at a higher temperature and is likely due to slow oxidation of unburned hydrocarbon residues that were not fully reacted in the initial exothermic event.

DSC analysis of solutions with increasing fuel concentrations ( $\varphi =$ 0.50-0.70) show similar thermal events as in the stock solution (Fig. 1B). Table 1 summarizes the peak temperatures and the heat released/consumed for all thermal events. Upon adding C5H8O2 fuel, the center of the endothermic solvent evaporation peak shifts from 391 to  ${\sim}400$  K for all  $\phi$  values. The consumed heat also increases from 270 (  $\phi$ = 0) to 398 J  $g^{-1}$  ( $\phi$  = 0.5 or 0.6), followed by a slight decrease to 388 J  $g^{-1}$  ( $\phi=0.7$ ). Incorporating  $C_5H_8O_2$  into the solutions also shifts the  $\alpha$ peak position from 427 to 440 K. There are no major changes of the shape or position of the  $\alpha$  peaks for all  $C_5H_8O_2$ -containing solutions with increasing  $\phi$  values. However, these solutions release more heat (161–171 J g $^{-1}$ ) at the  $\alpha$  peak than the stock solution (121 J g $^{-1}$ ). The broad exothermic  $\beta$  peak has a tail, indicating the initial ignition of carbon-based residues, followed by slower smoldering of the material at slightly higher temperatures. The released energy for this step increases first with the  $\varphi$  value and then decreases. The position of the  $\beta$  peak appears to shift inconsistently as the C<sub>5</sub>H<sub>8</sub>O<sub>2</sub> concentration increases.

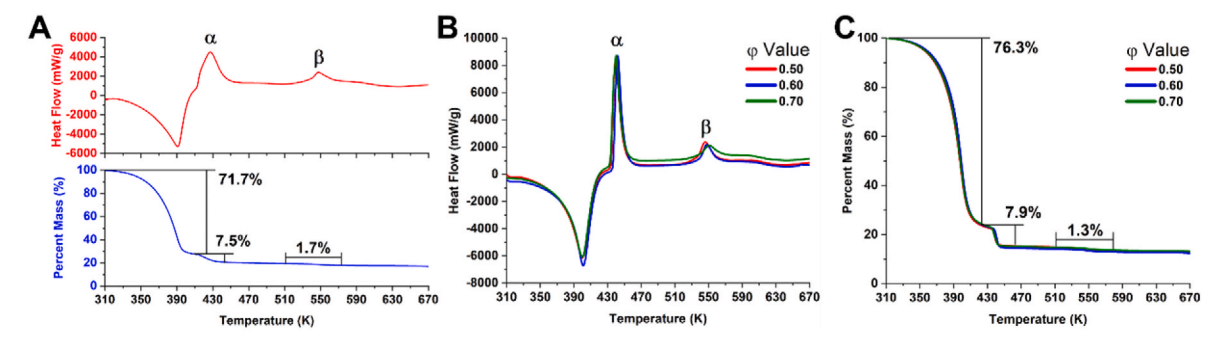


Fig. 1. DSC-TGA plots for the  $Eu(NO_3)_3 + 2$ -methoxyethanol (A), DSC (B) and TGA (C) plots for  $Eu(NO_3)_3 + \varphi C_5 H_8 O_2 + 2$ -methoxyethanol solutions with different  $\varphi$  values.

**Table 1** DSC peak positions (T) and heat released/consumed for the  $Eu(NO_3)_3 + \varphi C_5 H_8 O_2 + 2$ -methoxyethanol solutions.

	Endotherm Peak		Alpha Peak (α)		Beta Peak (β)	
φ	T (K)	Heat (J•g <sup>-1</sup> )	T (K)	Heat (J•g <sup>-1</sup> )	T (K)	Heat (J•g <sup>-1</sup> )
0	391	270	427	-121	546	-47
0.5	400	398	440	-168	546	-56
0.6	400	398	440	-161	548	-44
0.7	400	388	440	-171	550	-28

These slight variations in the peak centers may be due to the differences in concentrations of unburned hydrocarbon residues. Corresponding TGA curves (Fig. 1C) show that all  $C_5H_8O_2\text{-containing}$  solutions follow similar patterns of mass loss, with solvent evaporation accounting for a 76.3% loss, while  $\alpha$  and  $\beta$  events resulting in 7.9% and 1.3% mass loss, respectively.

## 3.2. Combustion process

Fig. 2A shows several frames of representative high-speed imaging of

the combustion reaction for the  $Eu(NO_3)_3 + \varphi C_5 H_8 O_2 + 2$ -methoxyethanol precursor gel with  $\varphi = 0$  in air. The ignition delay time of this precursor is ~148 s on a hot plate at 773 K. These images show the formation of a large flame above the reacting sample. Using multiple thermocouples, time-temperature profiles of the process were measured on the precursor's surface at 1 and 2 cm above the surface. Fig. 2B-D shows representative profiles for C5H8O2-containing gels in air and nitrogen atmospheres and Eu<sub>2</sub>O<sub>3</sub>-diluted gels. The maximum temperature  $(T_m)$  for the  $Eu(NO_3)_3 + 0.5C_5H_8O_2 + 2$ -methoxyethanol gel was observed above the sample within the flame rather than closer to the surface (Fig. 2B). Precursor gels diluted with its solid product (Eu<sub>2</sub>O<sub>3</sub>) showed a smaller flame than undiluted gels and relatively higher T<sub>m</sub> closer to the sample's surface (Fig. 2C). The combustion of gels with  $\phi =$ 0.5 under nitrogen exhibited no flame with the rapid expansion of a dark-grey porous solid due to the unburned organic residues. This result confirms that the  $\beta$  peak on DSC plots is the oxidation of unburned organic residues. The temperature profiles measured at the surface of the samples reacted in nitrogen atmosphere are similar to that shown in Fig. 2D.

Table 2 summarizes measured  $T_m$ , heating and cooling rates determined from temperature profiles for samples reacted in different conditions. Under both atmospheres, increasing  $\phi$  also increases  $T_m$  by

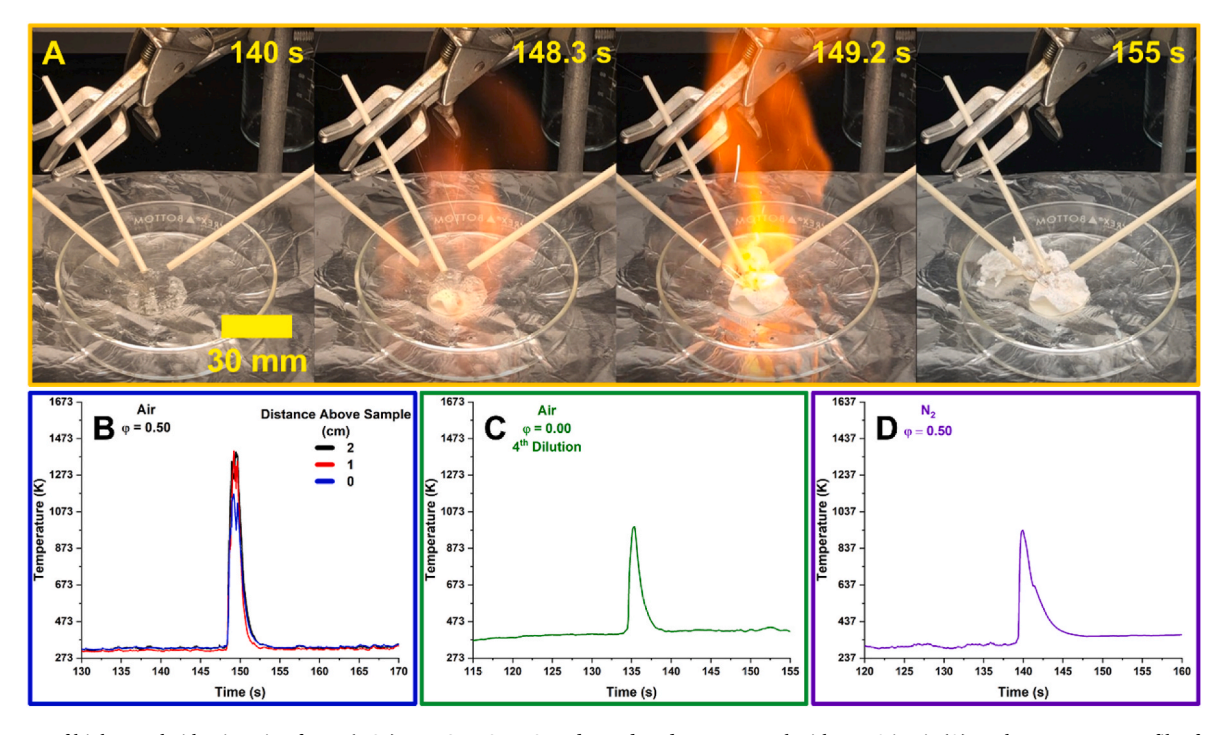


Fig. 2. Frames of high-speed video imaging for  $Eu(NO_3)_3 + \varphi C_5 H_8 O_2 + 2$ -methoxyethanol precursor gel with  $\varphi = 0$  in air (A), and temperature profiles for gel with  $\varphi = 0.5$  combusted in the air (B),  $Eu_2O_3$ -diluted gel with  $\varphi = 0$  combusted in the air (C) and gel with  $\varphi = 0$  in the nitrogen (D).

**Table 2** The measured maximum combustion temperature  $(T_m)$  on the gel surface, the heating and cooling rates of products for the Eu(NO<sub>3</sub>)<sub>3</sub> +  $\phi$ C<sub>5</sub>H<sub>8</sub>O<sub>2</sub> (Eu<sub>2</sub>O<sub>3</sub>) + 2-methoxyethanol gels reacted in air and nitrogen.

Atmosphere	φ	Dilution	T <sub>m</sub> (K)	Heating rate (K•s <sup>-1</sup> )	Cooling rate (K•s <sup>-1</sup> )
Air	0	No	870	1000	400
	0	Yes	990	1530	375
	0.5	No	1169	2850	650
Nitrogen	0	No	722	770	110
	0.5	No	971	2570	260

 $\sim\!\!250\text{--}300$  K, while  $T_m$  values in air are 150–200 K higher than for the corresponding  $\phi$  values for the samples reacted in nitrogen. These results are consistent with DSC analysis, showing that the addition of  $C_5H_8O_2$  increases the energy output of the  $\alpha$  exothermic peak (Table 1). Heating rates under the nitrogen atmosphere are  $\sim\!\!250$  K s $^{-1}$ , which is lower than the samples with equivalent  $\phi$  values combusted in air.

Although the gel ( $\phi=0$ ) diluted with  $Eu_2O_3$  exhibits smaller flame sizes, the average  $T_m$  is 990 K, and heating rates measured on the precursor's surface are higher than those corresponding to the undiluted solutions. The dilution of gel with the product reduces the overall thermal output of the process. However, the presence of the inert solid increases the heat conduction in the reacting gels, thus increasing the  $T_m$  measured closer to the precursor's surface. Under a nitrogen atmosphere, the cooling of the products is slower (Table 2) than the

corresponding samples reacted in air. Two factors can explain this result: the slightly different thermal conductivity of nitrogen (26.0 mW/m $\bullet$ K) and air (26.2 mW/m $\bullet$ K) and better thermal dissipation in the open air compared to the reaction vessel.

We also conducted spraying-assisted SCS of Eu<sub>2</sub>O<sub>3</sub> on silicon and aluminum substrates. The  $Eu(NO_3)_3+\phi C_5H_8O_2+2$ -methoxyethanol solutions ( $\phi=0.5$  or 0.6) were sprayed on the substrate, followed by heat treatments at 623, 673, or 873 K. The combustion of thin layers of solutions generates little heat and limits the temperature of the sample to be closer to the furnace temperature. This spray-assisted SCS enables preparing dispersed materials and films on the substrate.

## 3.3. Structure and composition of materials

Energy dispersive X-ray spectroscopy analysis of bulk samples prepared by air combustion shows no major contaminants within the produced sample (Fig. S2). PXRD patterns for bulk samples prepared with a  $\phi=0$  precursor in air are mixtures of cubic (C–Eu<sub>2</sub>O<sub>3</sub>) and monoclinic (B–Eu<sub>2</sub>O<sub>3</sub>) crystalline Eu<sub>2</sub>O<sub>3</sub> phases (Fig. 3A). Increasing the fuel concentration to  $\phi=0.6$  increases  $T_m$  values and decreases the quantity of the C–Eu<sub>2</sub>O<sub>3</sub> phase in the sample obtained in air. Measured  $T_m$  for the Eu (NO<sub>3</sub>) $_3+\phi C_5H_8O_2+2$ -methoxyethanol gels with higher  $\phi$  values are as high as 1400 K, which is above the range of the reported temperatures (1348–1473 K) for the C–Eu<sub>2</sub>O<sub>3</sub>  $\rightarrow$  B–Eu<sub>2</sub>O<sub>3</sub> transition [21,27,29]. Earlier work has shown that this phase transition is kinetically limited and requires hours of annealing to convert C–Eu<sub>2</sub>O<sub>3</sub> into B–Eu<sub>2</sub>O<sub>3</sub> [30].

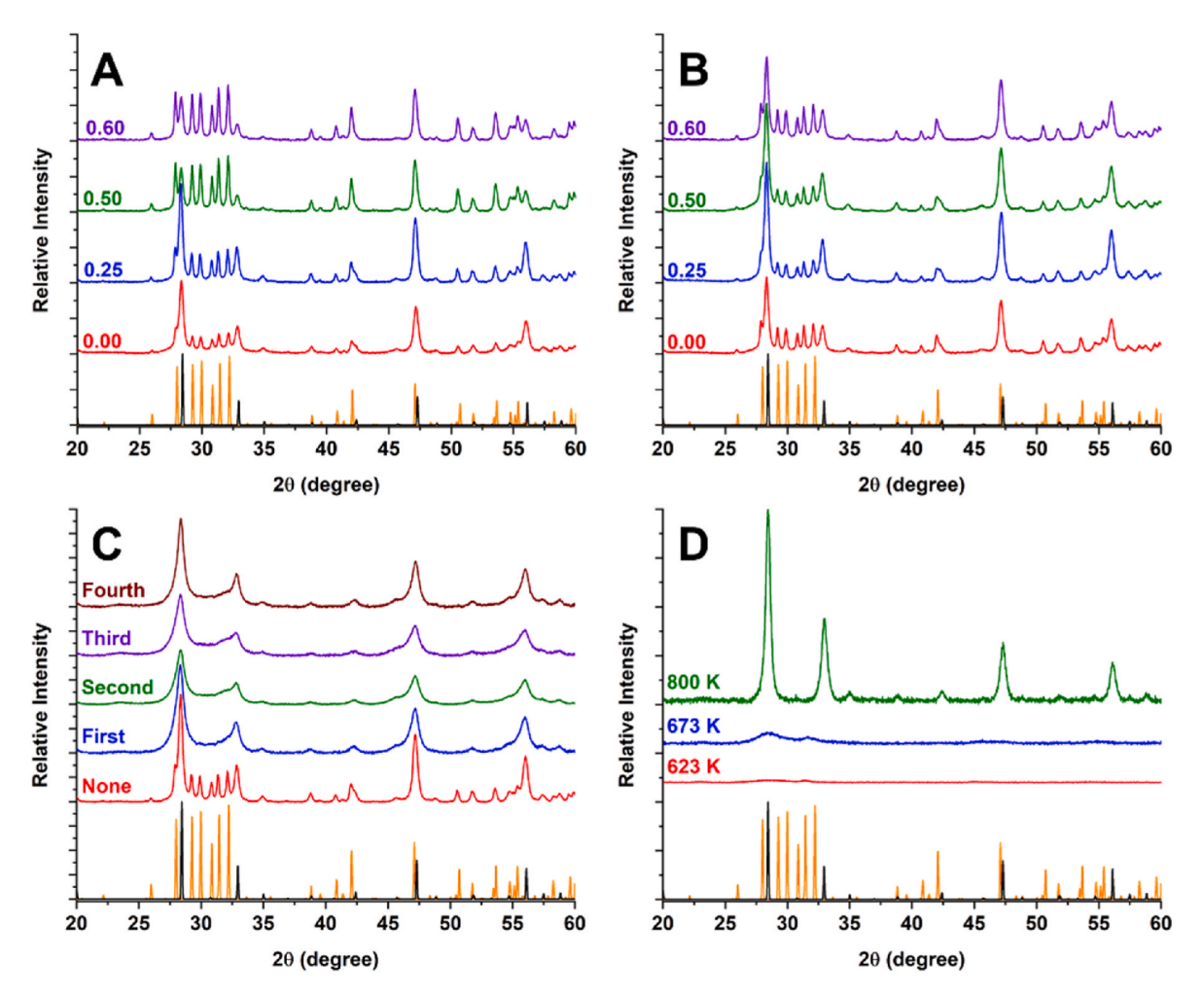


Fig. 3. PXRD patterns for products of the  $Eu(NO_3)_3 + \phi C_5H_8O_2 + 2$ -methoxyethanol gels combusted in the air (A), nitrogen (B), and consecutive 10% dilution with  $Eu_2O_3$  for precursor ( $\phi = 0$ ) (C). XRD patterns of sprayed  $Eu_2O_3$  on Si backing at increasing temperatures (D). Reference patterns for C– $Eu_2O_3$  (PDF# 01-083-7117) and B– $Eu_2O_3$  (PDF# 00-043-1009) are black and orange, respectively.

It is noteworthy that at  $\phi=0.6,~B-Eu_2O_3$  is dominant (~60%) in the product prepared during a short SCS. The material is heated for only seconds at or above the C  $\rightarrow$  B transition temperature during combustion. This brief heating seems to be enough to form the nanoscale high-temperature  $B-Eu_2O_3$  phase. At the same time, fast cooling in the post-combustion stage quenches the  $B-Eu_2O_3$  phase and limits its transition to C–Eu $_2O_3$ . Rietveld refinement of PXRD patterns (Fig. S3) shows a decrease in the amount of C–Eu $_2O_3$  from 80.6% at  $\phi=0$  to ~40% at  $\phi=0.6$  (Table 3).

The reaction products of identical precursors under a nitrogen atmosphere are also mixtures of two phases, with the C–Eu<sub>2</sub>O<sub>3</sub> portion changing from 65.2 to 72.2% (Fig. 3B). Notably, the  $T_m$  values for samples reacted in nitrogen are lower than previously reported  $C \leftrightarrow B$  transition temperatures. This result shows that the unique SCS conditions permit the formation of high-temperature phases at much lower temperatures. Fig. S4 shows Rietveld refinement patterns of Eu<sub>2</sub>O<sub>3</sub> produced under N<sub>2</sub>.

Reduced flame temperatures hinder the formation of  $B-Eu_2O_3$  at the combustion of diluted gels. After a single dilution,  $C-Eu_2O_3$  peaks in powder diffraction patterns are slightly broadened (Fig. 3C). Although the distinctive peaks for the monoclinic phase are not observed, a higher-than-average background between the intense (222) and (400) peaks of the  $C-Eu_2O_3$  is attributed to the significant broadening of multiple peaks for  $B-Eu_2O_3$ . Further successive dilution with  $Eu_2O_3$  shows no peaks of  $B-Eu_2O_3$  or increased broadening of the  $C-Eu_2O_3$  peaks.

XRD patterns of samples prepared by spraying reactive solutions, followed by annealing at 623 K, reveal a material with an amorphous structure, which develops some long-range order upon increasing the annealing temperature to 673 K (Fig. 3D). The diffraction pattern of a sample annealed at 873 K shows only peaks for C–Eu<sub>2</sub>O<sub>3</sub> and none for B–Eu<sub>2</sub>O<sub>3</sub>. This result suggests that, unlike bulk combustion, the spraying-assisted process enables better control over the temperature and prevents the formation of the B–Eu<sub>2</sub>O<sub>3</sub> phase.

## 3.4. Morphology

We conducted detailed electron microscopy and BET/BJH investigations to reveal the morphological and structural features of the prepared materials. Fig. 4 shows bright-field TEM and electron diffraction patterns for selected products. Fig. 4A–D are for the air combustion product of a precursor with  $\varphi = 0$ , while Fig. 4E-H and 4I - L are products for  $\varphi = 0.5$  precursors reacted in air and nitrogen, respectively. Without C<sub>5</sub>H<sub>8</sub>O<sub>2</sub> (Fig. 4A), products consist of agglomerates of interconnected porous structures. Porous morphologies were also observed after C<sub>5</sub>H<sub>8</sub>O<sub>2</sub> was added to the initial solutions. When combusted in air, the sample for  $\phi = 0.5$  precursors has a relatively lower porosity (Fig. 4E) than the other samples due to the higher T<sub>m</sub> resulting in sintering and pore collapse. The agglomerates for the products prepared under nitrogen (Fig. 4I) have relatively high porosity compared to the previous sample due to the lower T<sub>m</sub>. However, this porous morphology differs from the material produced by combustion of the  $\phi = 0$  precursor in air with a T<sub>m</sub> only lower by 100 K. This morphological difference is most likely due to the differences in heating rates between the two samples. A significantly higher heating rate would result in a more rapid

 $\label{eq:content_and_content} \begin{tabular}{ll} \textbf{Table 3} \\ \textbf{C}-Eu_2O_3 \ content \ determined \ via \ Rietveld \ refinement \ of PXRD \ patterns \ for the combustion of Eu(NO_3)_3 + \phi C_5H_8O_2 \ (Eu_2O_3) + 2\text{-methoxyethanol bulk precursors in \ different \ atmospheres.} \end{tabular}$ 

φ	Air	Nitrogen
0.00	80.6	72.2
0.25	67.4	65.2
0.50	38.3	73.7
0.60	40.0	65.5

release of gaseous products and, therefore, an expansion of the overall volume of pores due to the rapid pressure buildup.

Nitrogen physisorption analysis of the samples supports the bright-field TEM observations. All three samples exhibit type II adsorption/desorption isotherms with type H3 hysteresis loops (Fig. S5). This can be attributed to the plate-like particle aggregates that form slit-like pores. Table S1 shows calculated BET surface areas and BJH average adsorption pore sizes for all three samples. When combusted in air without fuel, materials have a surface area of  $\sim\!26~\text{m}^2/\text{g}$  and an average pore size of 24.9 nm. With the addition of fuel, there is a significant decrease in surface area to  $12~\text{m}^2/\text{g}$ , while the average pore size increases to 37.8 nm. These changes are the result of sintering. As the material is sintered at higher temperatures, mass diffusion causes pore size to increase. When the sample is combusted under a nitrogen atmosphere, a surface area of  $\sim\!25~\text{m}^2/\text{g}$  is achieved, similar to that obtained in the absence of fuel in air. However, a slight increase in the average pore size to 26.7 nm is observed compared to the  $\phi=0$  sample.

Images for all materials at higher magnification show highly crystalline particles with well-defined boundaries. Measured d-spacings of high-resolution TEM images match well (<5% error) with both the (310) and (111) planes of B–Eu $_2$ O $_3$ . This result supports the additional presence of the monoclinic phase. Electron diffraction patterns of all three materials show bright diffraction rings with d-spacings aligning well with that of C–Eu $_2$ O $_3$ . The diffraction rings corresponding to B–Eu $_2$ O $_3$  are not clearly visible. The most intense peaks for B–Eu $_2$ O $_3$  occur between the (222) and (400) reflections of C–Eu $_2$ O $_3$ . The lower sensitivity of the electron diffraction method as compared to XRD makes the distinction of the B–Eu $_2$ O $_3$  peaks between intense C–Eu $_2$ O $_3$  lines challenging.

The samples prepared by combustion of sprayed  $Eu(NO_3)_3$  +  $0.6C_5H_8O_2 + 2$ -methoxyethanol solution on untreated silicon wafers exhibit well-defined hemispheric-shaped particles across the substrate (Fig. 5A). Particle size distribution analysis using ImageJ software revealed that  $\sim$ 85% of the measured hemispheres (n = 1903) are within the range of 50–200 µm<sup>2</sup> (Fig. 5B). Similar hemispheric morphologies have been previously reported from 2-methoxyethanol-based solutions in the inkjet printing of metal oxide thin-film transistors [55]. Hexamethyldisilazane (HMDS) as a surface treatment agent changed the surface coverage [56,57]. To explore this possibility with a reactive solution, silicon wafers were coated with HMDS before spraying. The resulting materials show similar hemispheric morphologies to the first sprayed sample. However, size distribution analysis reveals that 98% of the measured hemispheres (n = 3925 and 2112, respectively) are in the range of 10–60 μm<sup>2</sup> (Fig. 5B). Thus, HMDS influences the formation of hemispheres on the substrate surface by decreasing the average size of the produced hemispheres. These results agree with similar trends reported by Wu et al., in which drops of aqueous In:Ga:Zn nitrate solutions inkjet-printed on SiO2 decreased in size and spacing when treated with HMDS compared to ozone pretreatment or without any pretreatment

Aluminum was also used as a substrate to deposit Eu<sub>2</sub>O<sub>3</sub> by spraying  $Eu(NO_3)_3 + 0.6C_5H_8O_2 + 2$ -methoxyethanol solution followed by annealing. Initial Al alloy samples were subjected to different surface pretreatments. Oxygen plasma cleaning of the substrate for 15 min improved solution spreading. However, the deposited layers are heavily cracked and detached from the substrate (Fig. S6). In addition, large circular areas contain no sprayed material. An Al substrate annealed at 573 K for 30 min followed by ozone pretreatment for 20 min allows the solution to uniformly spread across the surface with less damaged areas (Fig. 6A), as opposed to the plasma-cleaned Al substrate. The surface appears rough, with cracks and small bubble-like features. An identical surface treatment but using a solution with a  $\phi=0.5$  ratio results in smoother material but with areas of significant film detachment throughout the samples (Fig. 6B). Finally, changing the  $Eu(NO_3)_3$  concentration for the  $\varphi = 0.5$  solutions enables tuning of the surface coverage of the material. Increasing the solution concentration to 1 M

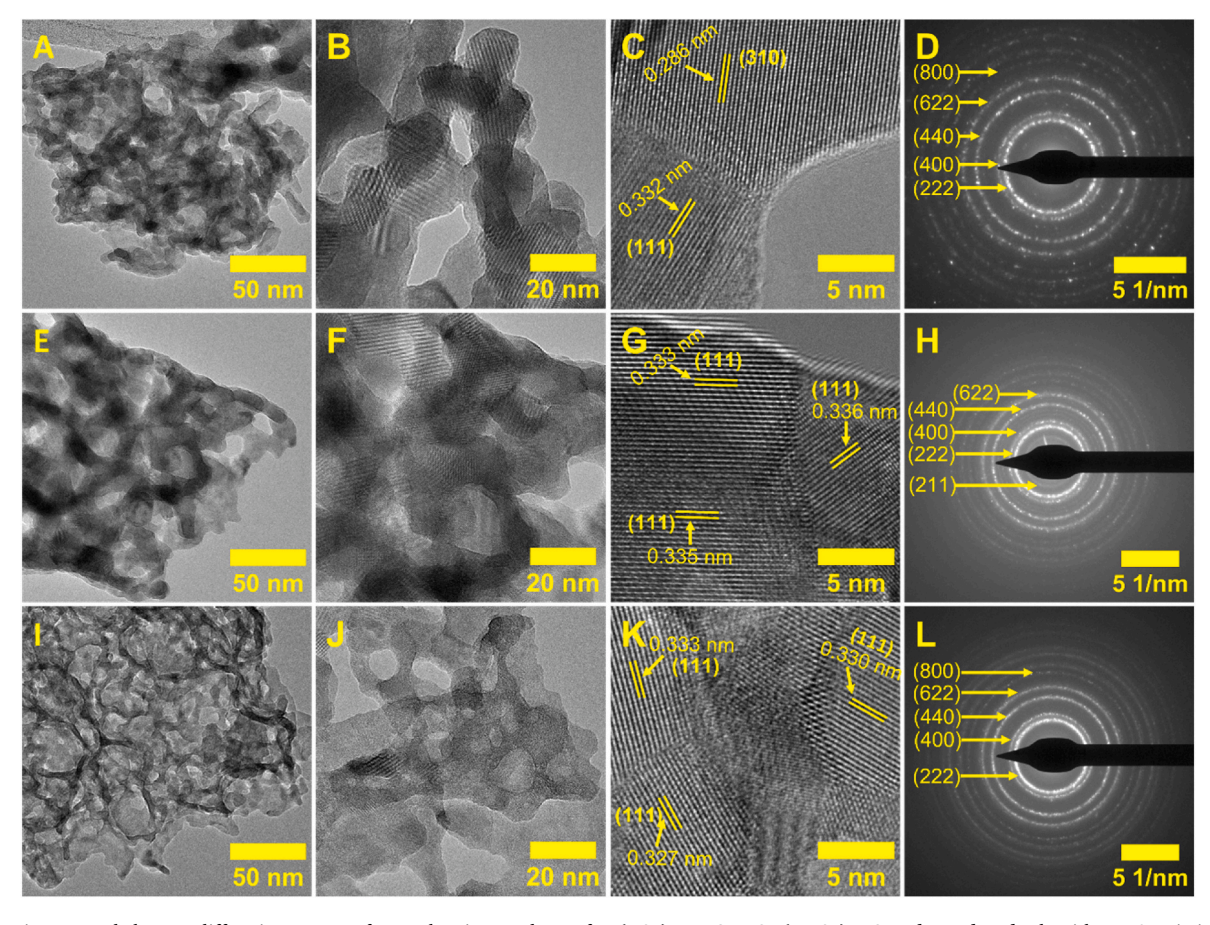


Fig. 4. TEM images and electron diffraction patterns for combustion products of  $Eu(NO_3)_3 + \varphi C_5H_8O_2$  ( $Eu_2O_3$ ) + 2-methoxyethanol gels with  $\varphi = 0$  ratio in air (A–D), and  $\varphi = 0.5$  reacted in air (E–H) and nitrogen (I–L).

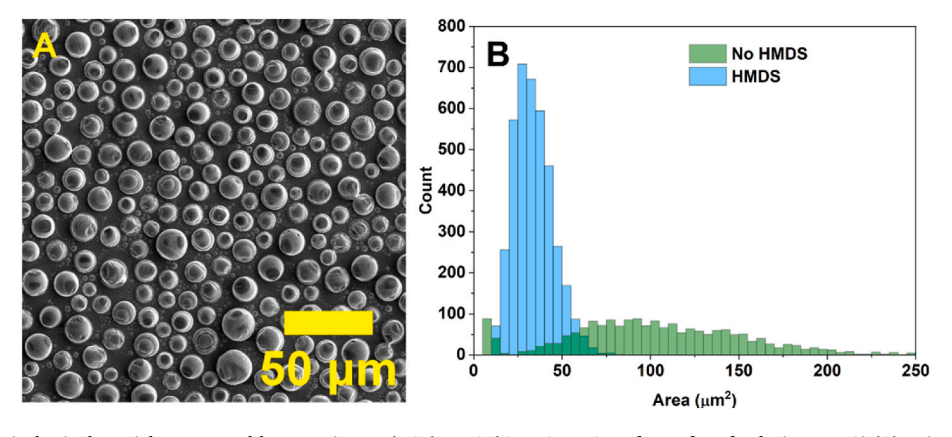


Fig. 5. SEM image of hemispherical particles prepared by spraying  $Eu(NO_3)_3 + 0.6C_5H_8O_2 + 2$ -methoxyethanol solutions on Si (A). Histogram of particle sizes for samples with and without HMDS pretreatment (B).

europium nitrate leads to a rough surface morphology (Fig. 6C), while reducing the concentration to 0.25 M results in a thin film with minimal roughness (Fig. 6D). Cross-sectional SEM imaging of the produced film shows average thickness of 140  $\pm$  4 nm with no visible defects (Fig. 6F).

## 4. Conclusions

This work reports rapid solution combustion synthesis of nanoscale  $Eu_2O_3$  using  $Eu(NO_3)_3+\phi C_5H_8O_2+2$ -methoxyethanol solutions. Thermal analysis shows that 2-methoxyethanol acts as a reducing fuel without  $C_5H_8O_2$ . Upon adding  $C_5H_8O_2$ , the system releases more heat

during the combustion process. All tested solutions exhibit an intense heat release stage and less exothermic secondary process associated with the slow oxidation of unburned organic residues.

The combustion products formed in air are a mixture of cubic and monoclinic  $Eu_2O_3$  phases, with concentrations of the latter increasing with  $\phi$ . When combusted under nitrogen, the lack of external oxygen decreases the overall reaction temperature, hindering the formation of the high-temperature monoclinic phase. The dilution of reacting gels with  $Eu_2O_3$  product powders reduces the overall thermal output, lowering the flame temperature and content of monoclinic  $Eu_2O_3$ . TEM imaging shows that all powdered materials produced are highly porous

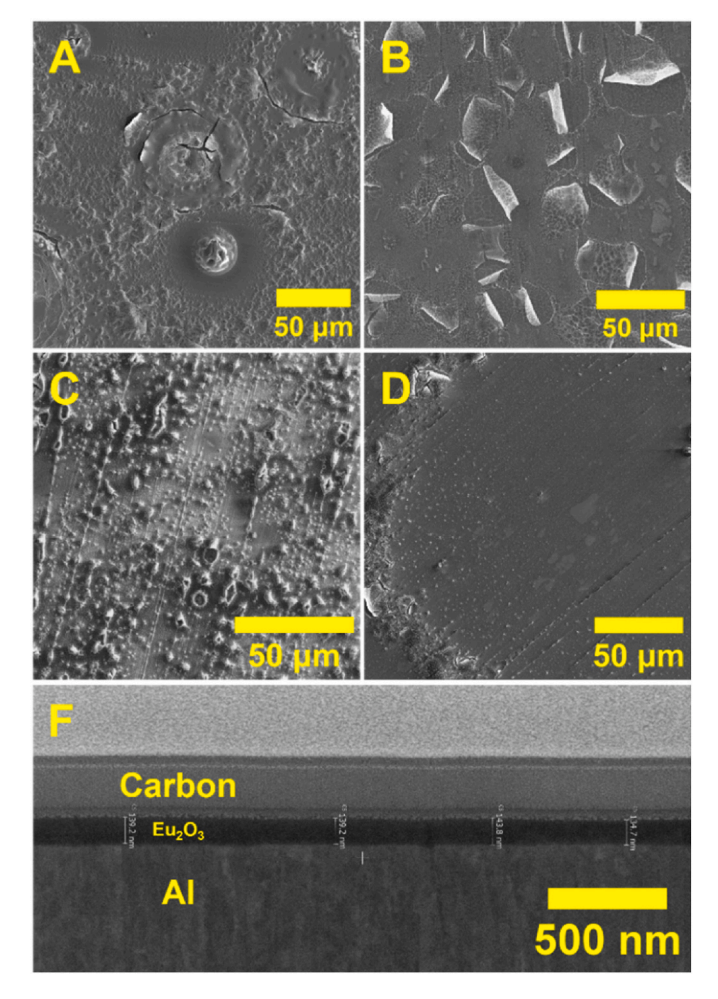


**Fig. 6.** SEM images for Eu<sub>2</sub>O<sub>3</sub> deposited on the aluminum substrate prepared with a 0.5 M  $\phi=0.6$  solution (A), 0.5 M  $\phi=0.5$  solution (B), 1 M  $\phi=0.5$  solution (C), and 0.25 M  $\phi=0.5$  solutions (D). Cross-sectional SEM image of the thin film prepared with 0.25 M  $\phi=0.5$  solution (F).

aggregates of crystalline nanoparticles. Changes to the  $\phi$  ratio and the reaction atmosphere influences the porosity of the products.

Monoclinic  $\mathrm{Eu_2O_3}$  can be produced even in an inert atmosphere or with dilution, indicating that rapid combustion allows for the easy preparation of nanoscale materials at lower temperatures than traditional synthesis methods. The results mentioned above are significant as they can help in producing monoclinic oxide phases of lanthanide series oxides at a faster rate. This can be useful for producing other materials. In order to prepare pure-phase bulk monoclinic oxides, future studies should focus on developing additional methods to regulate the combustion process.

In contrast to the bulk combustion of precursor gels, the thin-film combustion process produces pure cubic  $Eu_2O_3$ . Silicon and aluminum substrates are used in thin-film combustion while allowing tuning of the morphologies of the resulting materials. Electrospraying of solutions onto silicon substrates forms materials with hemispherical particle morphologies. A liquid-phase pretreatment of the surface narrows the size distribution of these particles. The combustion of solutions with a reduced concentration of  $Eu(NO_3)_3$  onto an Al substrate leads to the formation of thin films, particularly useful in target applications for nuclear science measurements, catalysis, and electronics research.

## CRediT authorship contribution statement

**Jordan M. Roach:** Investigation, Methodology, Data curation, Formal analysis, Writing – original draft. **Khachatur V. Manukyan:** 

Conceptualization, Methodology, Investigation, Writing – review & editing, Funding acquisition, Project administration. **Stefania Dede:** Investigation, Formal analysis, Writing – original draft. **Peter C. Burns:** Methodology, Writing – review & editing. **Ani Aprahamian:** Supervision, Writing – review & editing, Funding acquisition, Project administration.

## Declaration of competing interest

The authors declare that they have no known competing financial interests or personal relationships that could have appeared to influence the work reported in this paper.

#### Data availability

No data was used for the research described in the article.

## Acknowledgments

The work was performed with financial support from the U.S. Department of Energy's (DOE) National Nuclear Security Administration, USA (NNSA, Grant # NA0004093) and the U.S. National Science Foundation (NSF, PHY 2011890). This work is partly supported by U.S. Army Research Office Grant #W911NF2110045 under the Materials Synthesis & Processing Program, with Dr. Michael P. Bakas as the program manager. The authors also acknowledge Grace Arntz-Johnson for the help in obtaining BET surface area data and Notre Dame Center for Environmental Science & Technology (CEST) and Integrated Imaging Facility (NDIIF) for instrumentation usage.

## Appendix A. Supplementary data

Supplementary data to this article can be found online at https://doi. org/10.1016/j.jssc.2023.124235.

### References

- [1] R. Liu, M. Buchert, S. Dittrich, A. Manhart, C. Merz, D. Schüler, Application of rare earths in consumer electronics and challenges for recycling, in: 2011 IEEE International Conference on Consumer Electronics -Berlin, 2011, pp. 286–290, https://doi.org/10.1109/ICCEBerlin.2011.6031826.
- [2] S.V. Eliseeva, J.C.G. Bünzli, Rare earths: jewels for functional materials of the future, New J. Chem. 35 (2011) 1165–1176, https://doi.org/10.1039/c0nj00969e.
- [3] S. Zhang, S.E. Saji, Z. Yin, H. Zhang, Y. Du, C.H. Yan, Rare-earth incorporated alloy catalysts: synthesis, properties, and applications, Adv. Mater. 33 (2021), 2005988, https://doi.org/10.1002/adma.202005988.
- [4] M.K. Hossain, M.I. Khan, A. El-Denglawey, A review on biomedical applications, prospects, and challenges of rare earth oxides, Appl. Mater. Today 24 (2021), 101104, https://doi.org/10.1016/j.apmt.2021.101104.
- [5] J.M.D. Coey, Perspective and prospects for rare earth permanent magnets, Engineering 6 (2020) 119–131, https://doi.org/10.1016/j.eng.2018.11.034.
- [6] S. Sugimoto, Current status and recent topics of rare-earth permanent magnets, J. Phys. D Appl. Phys. 44 (2011), 064001, https://doi.org/10.1088/0022-3727/ 44/6/064001.
- [7] A.V. Gelis, G.J. Lumetta, Actinide lanthanide separation process ALSEP, Ind. Eng. Chem. Res. 53 (2014) 1624–1631, https://doi.org/10.1021/ie403569e.
- [8] A. Geist, J.M. Adnet, S. Bourg, C. Ekberg, H. Galán, P. Guilbaud, M. Miguirditchian, G. Modolo, C. Rhodes, R. Taylor, An overview of solvent extraction processes developed in europe for advanced nuclear fuel recycling, part 1 heterogeneous recycling, Separ. Sci. Technol. 56 (2021) 1866–1881, https://doi.org/10.1080/01496395.2020.1795680.
- [9] K. Niu, F. Yang, T. Gaudin, H. Ma, W. Fang, Theoretical study of effects of solvents, ligands, and anions on separation of trivalent lanthanides and actinides, Inorg. Chem. 60 (2021) 9552–9562, https://doi.org/10.1021/acs.inorgchem.1c00657.
- [10] A. Ikeda, T. Suzuki, M. Aida, Y. Fujii, T. Mitsugashira, M. Hara, M. Ozawa, Chromatographic separation of trivalent actinides and rare earth elements by using pyridine type resin, J. Radioanal. Nucl. Chem. 263 (2005) 605–611.
- [11] V. Balaram, Rare earth elements: a review of applications, occurrence, exploration, analysis, recycling, and environmental impact, Geosci. Front. 10 (2019) 1285–1303, https://doi.org/10.1016/j.gsf.2018.12.005.
- [12] S. Bourg, C. Poinssot, Could spent nuclear fuel be considered as a non-conventional mine of critical raw materials? Prog. Nucl. Energy 94 (2017) 222–228, https://doi. org/10.1016/j.pnucene.2016.08.004.
- [13] J. Bruno, R.C. Ewing, Spent nuclear fuel, Elements 2 (2006) 343–349. http://pubs.geoscienceworld.org/msa/elements/article-pdf/2/6/343/3111364/343\_v2n6.pdf.

- [14] W.D. Loveland, D.J. Morrissey, G.T. Seaborg, Modern Nuclear Chemistry, second ed., John Wiley & Sons, Inc., Hoboken, NJ, U.S.A., 2017 https://doi.org/10.1002/ 9781119348450
- [15] G. Arrachart, J. Couturier, S. Dourdain, C. Levard, S. Pellet-Rostaing, Recovery of rare earth elements (REEs) using ionic solvents, Processes 9 (2021) 1202, https://doi.org/10.3390/pr9071202.
- [16] D. Park, A. Middleton, R. Smith, G. Deblonde, D. Laudal, N. Theaker, H. Hsu-Kim, Y. Jiao, A biosorption-based approach for selective extraction of rare earth elements from coal byproducts, Sep. Purif. Technol. 241 (2020), 116726, https:// doi.org/10.1016/j.seppur.2020.116726.
- [17] Z. Chen, Z. Li, J. Chen, P. Kallem, F. Banat, H. Qiu, Recent advances in selective separation technologies of rare earth elements: a review, J. Environ. Chem. Eng. 10 (2022), 107104, https://doi.org/10.1016/j.jece.2021.107104.
- [18] B. Guo, A.S. Harvey, J. Neil, I.M. Kennedy, A. Navrotsky, S.H. Risbud, Atmospheric pressure synthesis of heavy rare earth sesquioxides nanoparticles of the uncommon monoclinic phase, J. Am. Ceram. Soc. 90 (2007) 3683–3686, https://doi.org/ 10.1111/j.1551-2916.2007.01961.x.
- [19] A. Quesada, A. del Campo, J.F. Fernández, Sintering behaviour and translucency of dense Eu<sub>2</sub>O<sub>3</sub> ceramics, J. Eur. Ceram. Soc. 34 (2014) 1803–1808, https://doi.org/ 10.1016/j.jeurceramsoc.2013.12.034.
- [20] J. Kaszewski, B.S. Witkowski, Ł. Wachnicki, H. Przybylińska, B. Kozankiewicz, E. Mijowska, M. Godlewski, Luminescence enhancement in nanocrystalline Eu<sub>2</sub>O<sub>3</sub> nanorods – microwave hydrothermal crystallization and thermal degradation of cubic phase, Opt. Mater. 59 (2016) 76–82, https://doi.org/10.1016/j.
- [21] C. Barad, G. Kimmel, H. Hayun, D. Shamir, K. Hirshberg, Y. Gelbstein, Phase stability of nanocrystalline grains of rare-earth oxides (Sm<sub>2</sub>O<sub>3</sub> and Eu<sub>2</sub>O<sub>3</sub>) confined in magnesia (MgO) matrix, Materials 13 (2020) 2201, https://doi.org/10.3390/ ma13092201
- [22] M.K. Hossain, M.H.K. Rubel, M.A. Akbar, M.H. Ahmed, N. Haque, M.F. Rahman, J. Hossain, K.M. Hossain, A review on recent applications and future prospects of rare earth oxides in corrosion and thermal barrier coatings, catalysts, tribological, and environmental sectors, Ceram. Int. 48 (2022) 32588–32612, https://doi.org/ 10.1016/j.ceramint.2022.07.220.
- [23] M.K. Hossain, S. Hossain, M.H. Ahmed, M.I. Khan, N. Haque, G.A. Raihan, A review on optical applications, prospects, and challenges of rare-earth oxides, ACS Appl. Electron. Mater. 3 (2021) 3715–3746, https://doi.org/10.1021/acsaelm.1c00682.
- [24] M.K. Hossain, M.H. Ahmed, M.I. Khan, M.S. Miah, S. Hossain, Recent progress of rare earth oxides for sensor, detector, and electronic device applications: a review, ACS Appl. Electron. Mater. 3 (2021) 4255–4283, https://doi.org/10.1021/ acsath\_1-00203
- [25] S. Bernal, G. Blanco, J.J. Calvino, J.A.P. Omil, J.M. Pintado, Some major aspects of the chemical behavior of rare earth oxides: an overview, J. Alloys Compd. 408–412 (2006) 496–502, https://doi.org/10.1016/j.jallcom.2004.12.090.
- [26] G. Azimi, R. Dhiman, H.M. Kwon, A.T. Paxson, K.K. Varanasi, Hydrophobicity of rare-earth oxide ceramics, Nat. Mater. 12 (2013) 315–320, https://doi.org/ 10.1038/nmat3545.
- [27] R.S. Roth, S.J. Schneider, Phase equilibria in systems involving the rare-earth oxides. part 1. polymorphism of the oxides of the trivalent rare-earth ions, J. Res. Natl. Bur. Stand. A Phys. Chem. 64A (1960) 309–316.
- [28] P.P. Fedorov, M.v. Nazarkin, R.M. Zakalyukin, On polymorphism and morphotropism of rare earth sesquioxides, Crystallogr. Rep. 47 (2002) 281–286, https://doi.org/10.1134/1.1466504.
- [29] G.-Y. Adachi, N. Imanaka, The binary rare earth oxides, Chem. Rev. 98 (1998) 1479–1514. https://pubs.acs.org/sharingguidelines.
- [30] M. Zinkevich, Thermodynamics of rare earth sesquioxides, Prog. Mater. Sci. 52 (2007) 597–647, https://doi.org/10.1016/j.pmatsci.2006.09.002.
- [31] K.P. Tseng, Q. Yang, S.J. McCormack, W.M. Kriven, High-entropy, phase-constrained, lanthanide sesquioxide, J. Am. Ceram. Soc. 103 (2020) 569–576, https://doi.org/10.1111/jace.16689.
- [32] M. Pianassola, K. Anderson, C. Agca, C.J. Benmore, J.W. McMurray, J. C. Neuefeind, C. Melcher, M. Zhuravleva, In situ high-temperature structural analysis of high-entropy rare-earth sesquioxides, Chem. Mater. 35 (2023) 1116–1124, https://doi.org/10.1021/acs.chemmater.2c03088.
- [33] J. Łażewski, M. Sternik, P.T. Jochym, J. Kalt, S. Stankov, A.I. Chumakov, J. Göttlicher, R. Rüffer, T. Baumbach, P. Piekarz, Lattice dynamics and structural phase transitions in Eu<sub>2</sub>O<sub>3</sub>, Inorg. Chem. 60 (2021) 9571–9579, https://doi.org/ 10.1021/acs.inorgchem.1c00708.
- [34] J.P. Lehtiö, T. Hadamek, M. Kuzmin, P. Laukkanen, A.A. Demkov, Evidence for the Eu 4f character of conduction-band edge at the Eu<sub>2</sub>O<sub>3</sub> surface studied by scanning tunneling spectroscopy, Surf. Sci. 705 (2021), 121763, https://doi.org/10.1016/j. susc 2020.121763
- [35] J. Lai, T. Wang, H. Zhang, L. Ye, C. Yan, W. Gu, Modulating the photoluminescence of europium oxide nanoparticles by controlling thermal decomposition conditions, J. Lumin. 214 (2019), 116534, https://doi.org/10.1016/j.jlumin.2019.116534.
- [36] S. Kumar, R. Prakash, R.J. Choudhary, D.M. Phase, Structural, morphological and electronic properties of pulsed laser grown Eu<sub>2</sub>O<sub>3</sub> thin films, AIP Conf. Proc. 1953 (2018), 100012, https://doi.org/10.1063/1.5032948.
- [37] A. Varma, A.S. Mukasyan, A.S. Rogachev, K.V. Manukyan, Solution combustion synthesis of nanoscale materials, Chem. Rev. 116 (2016) 14493–14586, https:// doi.org/10.1021/acs.chemrev.6b00279.

- [38] S.L. González-Cortés, F.E. Imbert, Fundamentals, properties and applications of solid catalysts prepared by solution combustion synthesis (SCS), Appl. Catal. Gen. 452 (2013) 117–131, https://doi.org/10.1016/j.apcata.2012.11.024.
- [39] L.A. Sani, C. Wang, M. Zhang, H. Bai, P. An, Z. Han, L. Shi, K. Wang, D. Bai, G. Xu, F. Su, Z. Zhang, Methanation of CO<sub>2</sub> over Yb-promoted Ni/Al<sub>2</sub>O<sub>3</sub> catalysts prepared by solution combustion, Energy Fuel. 36 (2022) 5360–5374, https://doi.org/10.1021/acs.energyfuels.2c00180.
- [40] O. Thoda, G. Xanthopoulou, G. Vekinis, A. Chroneos, Review of recent studies on solution combustion synthesis of nanostructured catalysts, Adv. Eng. Mater. 20 (2018), 1800047, https://doi.org/10.1002/adem.201800047.
- [41] H. Aali, N. Azizi, N.J. Baygi, F. Kermani, M. Mashreghi, A. Youssefi, S. Mollazadeh, J.V. Khaki, H. Nasiri, High antibacterial and photocatalytic activity of solution combustion synthesized Ni<sub>0.5</sub>Zn<sub>0.5</sub>Fe<sub>2</sub>O<sub>4</sub> nanoparticles: effect of fuel to oxidizer ratio and complex fuels, Ceram. Int. 45 (2019) 19127–19140, https://doi.org/10.1016/j.ceramint.2019.06.159
- [42] X. Wang, M. Qin, F. Fang, B. Jia, H. Wu, X. Qu, A.A. Volinsky, Effect of glycine on one-step solution combustion synthesis of magnetite nanoparticles, J. Alloys Compd. 719 (2017) 288–295, https://doi.org/10.1016/j.jallcom.2017.05.187.
- [43] N. Amirkhanyan, S. Kharatyan, K. Manukyan, A. Aprahamian, Thermodynamics and kinetics of solution combustion synthesis: Ni(NO<sub>3</sub>)<sub>2</sub> + fuels systems, Combust. Flame 221 (2020) 110–119, https://doi.org/10.1016/j. combustflame\_2020.07.038.
- [44] R.K. Lenka, T. Mahata, P.K. Sinha, A.K. Tyagi, Combustion synthesis of gadolinia-doped ceria using glycine and urea fuels, J. Alloys Compd. 466 (2008) 326–329, https://doi.org/10.1016/j.jallcom.2007.11.028.
- [45] C. Xu, K.V. Manukyan, R.A. Adams, V.G. Pol, P. Chen, A. Varma, One-step solution combustion synthesis of CuO/Cu<sub>2</sub>O/C anode for long cycle life Li-ion batteries, Carbon 142 (2019) 51–59, https://doi.org/10.1016/j.carbon.2018.10.016.
- [46] A.S. Mukasyan, S. Roslyakov, J.M. Pauls, L.C. Gallington, T. Orlova, X. Liu, M. Dobrowolska, J.K. Furdyna, K.V. Manukyan, Nanoscale metastable ε-Fe<sub>3</sub>N ferromagnetic materials by self-sustained reactions, Inorg. Chem. 58 (2019) 5583–5592, https://doi.org/10.1021/acs.inorgchem.8b03553.
- [47] S. Dede, K.V. Manukyan, J.M. Roach, A. Majumdar, P.C. Burns, A. Aprahamian, Irradiation-induced amorphization of UO<sub>2</sub> films prepared by spraying-assisted combustion synthesis, Appl. Surf. Sci. 603 (2022), 154437, https://doi.org/ 10.1016/j.apsusc.2022.154437.
- [48] A. Majumdar, K.V. Manukyan, S. Dede, J.M. Roach, D. Robertson, P.C. Burns, A. Aprahamian, Irradiation-driven restructuring of UO<sub>2</sub> thin films: amorphization and crystallization, ACS Appl. Mater. Interfaces 13 (2021) 35153–35164, https://doi.org/10.1021/acsami.1c08682.
- [49] J.M. Roach, K.V. Manukyan, A. Majumdar, S. Dede, A.G. Oliver, P.C. Burns, A. Aprahamian, Hyperstoichiometric uranium dioxides: rapid synthesis and irradiation-induced structural changes, Inorg. Chem. 60 (2021) 18938–18949, https://doi.org/10.1021/acs.inorgchem.1c02736.
- [50] A. Majumdar, K.V. Manukyan, W. Tan, S. Dede, J.M. Roach, A. Couture, P.C. Burns, A. Aprahamian, Neutron capture of UO<sub>2</sub> targets prepared by spin-coating assisted combustion synthesis, Nucl. Instrum. Methods Phys. Res. 1045 (2023), 167551, https://doi.org/10.1016/j.nima.2022.167551.
- [51] S. Dede, K.V. Manukyan, J.M. Roach, D. Robertson, P.C. Burns, A. Aprahamian, Irradiation-enhanced interaction at UO<sub>2</sub>/Al<sub>2</sub>O<sub>3</sub>/Al interfaces, J. Phys. Chem. C (2023) 9850–9857, https://doi.org/10.1021/acs.jpcc.3c01155.
- [52] A. Sil, E.A. Goldfine, W. Huang, M.J. Bedzyk, J.E. Medvedeva, A. Facchetti, Role of fluoride doping in low-temperature combustion-synthesized ZrO<sub>x</sub> dielectric films, ACS Appl. Mater. Interfaces 14 (2022) 12340–12349, https://doi.org/10.1021/ 202201116/219852
- [53] B. Wang, W. Huang, M.J. Bedzyk, V.P. Dravid, Y.Y. Hu, T.J. Marks, A. Facchetti, Combustion synthesis and polymer doping of metal oxides for high-performance electronic circuitry, Acc. Chem. Res. 55 (2022) 429–441, https://doi.org/10.1021/ acs.accounts.1c00671.
- [54] N. Doebelin, R. Kleeberg, Profex: a graphical user interface for the rietveld refinement program BGMN, J. Appl. Crystallogr. 48 (2015) 1573–1580, https://doi.org/10.1107/S1600576715014685.
- [55] D. Kim, Y. Jeong, K. Song, S.K. Park, G. Cao, J. Moon, Inkjet-printed zinc tin oxide thin-film transistor, Langmuir 25 (2009) 11149–11154, https://doi.org/10.1021/ la001436p.
- [56] F. Chiarella, M. Barra, L. Ricciotti, A. Aloisio, A. Cassinese, Morphology, electrical performance and potentiometry of PDIF-CN<sub>2</sub> thin-film transistors on HMDS-treated and bare silicon dioxide, Electronics 3 (2014) 76–86, https://doi.org/10.3390/ electronics3010076.
- [57] M.R. Fiorillo, C. Diletto, P. Tassini, M.G. Maglione, E. Santoro, F. Villani, R. Liguori, P. Maddalena, A. Rubino, C. Minarini, PC<sub>70</sub>BM n-type thin film transistors: influence of HMDS deposition temperature on the devices properties, Mater. Today: Proc. 3 (2016) 720–726, https://doi.org/10.1016/j. mator.2016.02.002.
- [58] S. Wu, Q. Zhang, Z. Chen, L. Mo, S. Shao, Z. Cui, Inkjet printing of oxide thin film transistor arrays with small spacing with polymer-doped metal nitrate aqueous ink, J. Mater. Chem. C Mater. 5 (2017) 7495–7503, https://doi.org/10.1039/ c7te11303e